Ultralow Density, Monolithic WS_2, MoS_2, and MoS_2/Graphene Aerogels

Marcus A. Worsley,* Swanee J. Shin, Matthew D. Merrill, Jeremy Lenhardt, Art J. Nelson, Leta Y. Woo, Alex E. Gash, Theodore F. Baumann, and Christine A. Orme

Lawrence Livermore National Laboratory, 7000 East Avenue, Livermore, California 94550, United States

ABSTRACT We describe the synthesis and characterization of monolithic, ultralow density WS_2 and MoS_2 aerogels, as well as a high surface area MoS_2/graphene hybrid aerogel. The monolithic WS_2 and MoS_2 aerogels are prepared via thermal decomposition of freeze-dried ammonium thio-molybdate (ATM) and ammonium thio-tungstate (ATT) solutions, respectively. The densities of the pure dichalcogenide aerogels represent 0.4% and 0.5% of full density MoS_2 and WS_2, respectively, and can be tailored by simply changing the initial ATM or ATT concentrations. Similar processing in the presence of the graphene aerogel results in a hybrid structure with MoS_2 sheets conformally coating the graphene scaffold. This layered motif produces a ~50 wt % MoS_2 aerogel with BET surface area of ~700 m^2/g and an electrical conductivity of 112 S/m. The MoS_2/graphene aerogel shows promising results as a hydrogen evolution reaction catalyst with low onset potential (~100 mV) and high current density (100 mA/cm^2 at 260 mV).

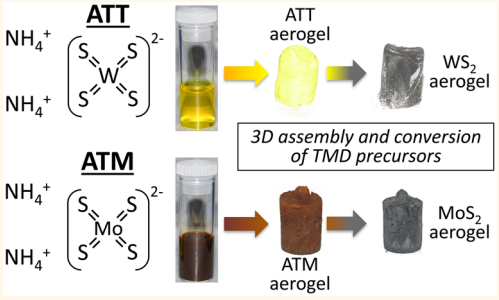

KEYWORDS: transition metal dichalcogenide (TMD) · 3D assembly · cryogel · 2D materials · graphene analogues · layered material · catalysis

Two-dimensional (2D), or layered materials (*e.g.*, graphene and graphene analogues) are relevant to a broad range of research fields and industrial processes.[1−19] Both graphene and graphene analogues, such as layered dichalcogenides (*e.g.*, MoS_2, WS_2, $MoSe_2$, $TiSe_2$, *etc.*), because of their exceptional properties, have been widely researched by physicists, chemists, and materials scientists for applications that include catalysis, energy storage, lubricants, sensors, and electronics.[1−20] Though graphene was initially limited to 2D sheets, in recent years there has been an explosion of reports on 3D graphene assemblies.[20−40] In contrast, while various chalcogenide aerogels[41] have been reported, literature on graphene analogues has been focused on nanoparticles or powders. Reports of monolithic assemblies of graphene analogues, such as boron nitride[42,43] and MoS_2,[44] remain extremely limited, and to our knowledge no monolithic WS_2 aerogels have been reported.

In this report, we describe the synthesis of ultralow density MoS_2 and WS_2 cryogels using thermal decomposition of traditional precursors, ammonium thio-metal salts. The critical factor in this method is the 3D assembly of the MoS_2 and WS_2 precursor. One must select a precursor that is both amenable to forming an extended 3D network structure during the assembly phase and maintaining this form upon drying and chemical conversion to the dichalcogenide product. In this case, ammonium thio-molybdate (ATM) and ammonium thio-tungstate (ATT) proved to be suitable precursors for the MoS_2 and WS_2 aerogels, respectively. Both can be cast into 3D assemblies *via* freeze-drying and both are common precursors for commercial production of MoS_2 and WS_2 catalysts *via* thermal decomposition.[45,46] The thermal decomposition of ATM and ATT to their respective sulfides (MS_2, where M = Mo or W) proceeds at 450 °C in hydrogen *via* the following reactions:

$$(NH_4)_2(MS_4) \rightarrow MS_3 + 2NH_3 + H_2S \quad (1)$$

$$MS_3 + H_2 \rightarrow MS_2 + H_2S \quad (2)$$

Therefore, the physical structure of the freeze-dried aerogels must be robust enough to undergo these high temperature chemical transformations without collapse, thus

* Address correspondence to worsley1@llnl.gov.

Received for review July 2, 2014 and accepted April 10, 2015.

Published online April 10, 2015
10.1021/acsnano.5b00087

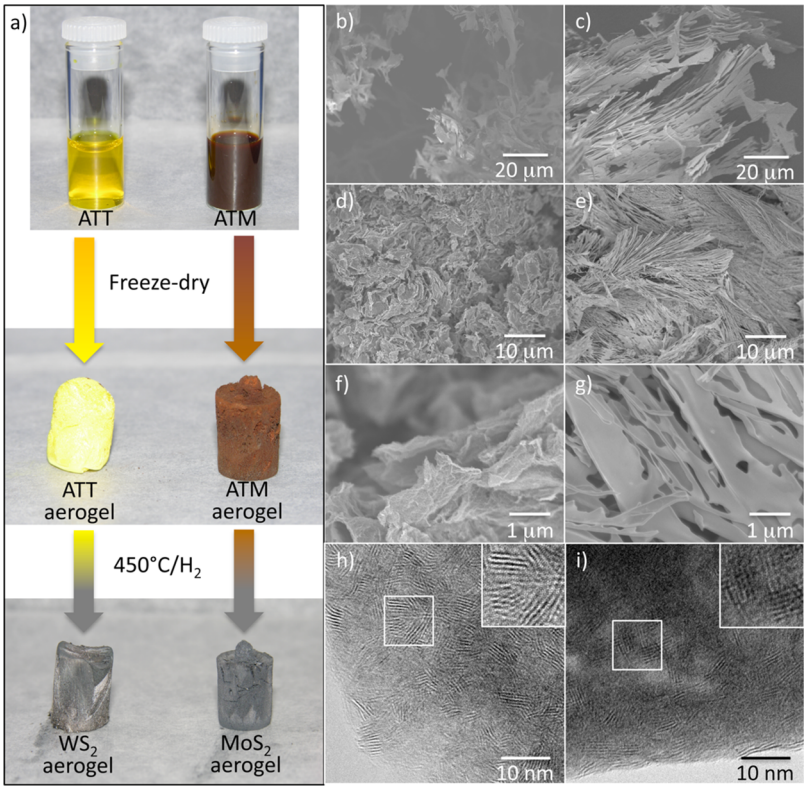

Figure 1. (a) Synthesis scheme for MoS_2 and WS_2 aerogels. SEM images of (b) ATM, (c) ATT, (d and f) MoS_2, and (e and g) WS_2 aerogels. TEM images of (h) MoS_2 and (i) WS_2 aerogels. The inset in images h and I is the magnification of the white box and is 10 nm in width.

transferring the architecture of the precursor aerogel to the reduced product. In this work, we describe a straightforward method to precursor aerogel assembly and chemical conversion to the layered dichalcogenide aerogels, as well as characterization of these novel low-density solids.

RESULTS/DISCUSSION

Figure 1a illustrates the scheme used to synthesize the ultralow density dichalcogenide aerogels. First, aqueous solutions of the ATM and ATT precursor were prepared. The precursor solutions were freeze-dried to create a stable 3D assembly. The ATT formed a bright yellow gel, while the ATM was a brownish-red monolith, reflecting the hues seen in the solutions. Next the precursor gels were annealed in hydrogen to produce the final silvery, gray MoS_2 and WS_2 aerogels. The density of the aerogels could be controlled *via* the concentration of precursor in the starting solution. For the MoS_2 aerogels, densities of 22, 27, and 56 mg/cm^3 (representing 0.4, 0.5, and 1.1% of the density of single crystal MoS_2, 5.06 g/cm^3) were observed for aqueous ATM concentrations of 13, 26, and 52 mg/ml, respectively. ATM solutions of 13 mg/ml and below experienced significant shrinkage upon freeze-drying placing a lower limit on dichalcogenide densities using this technique. The upper limit was not explored but it should coincide with the solubility limit of the precursor or one's ability to make a stable, homogeneous suspension before freezing. Similar observations were made for the ATT solutions. The densities of the WS_2 aerogels were 34 and 54 mg/cm^3 representing 0.5 and 0.7% of the density of single crystal WS_2 (7.5 g/cm^3). Despite their low density, Young's moduli of 35 $\pm$ 5 MPa were observed, which is comparable to values reported in analogous graphene aerogels.[33] However, unlike graphene aerogels, the chalcogenide aerogels' deformation had a significant plastic component (Supporting Information, Figure S1) similar to a shape-memory foam.[47]

Field emission scanning electron microscopy (FE-SEM) of the aerogels shows how the morphology of the precursor (ATM and ATT) foams defines the microstructure of the dichalcogenide aerogels. (Figure 1b−g) The ATM aerogels have a sheetlike architecture, commonly observed in 3D assemblies of other 2D materials (*e.g.*, graphene and boron nitride aerogels).[33,43,48] The sheets have varying degrees of curvature and are randomly oriented. This random sheetlike motif is maintained in the MoS_2 aerogels. However, the ATT aerogel, though random on the global scale, appears to have significant regions of locally aligned sheets. Furthermore, the sheets of the ATT foam appear to be much smoother and larger than those in the ATM aerogel. The diverse morphologies are likely due to differences in the crystallization of ATM and ATT during the freezing step. The smoother, larger flakes in the ATT precursor

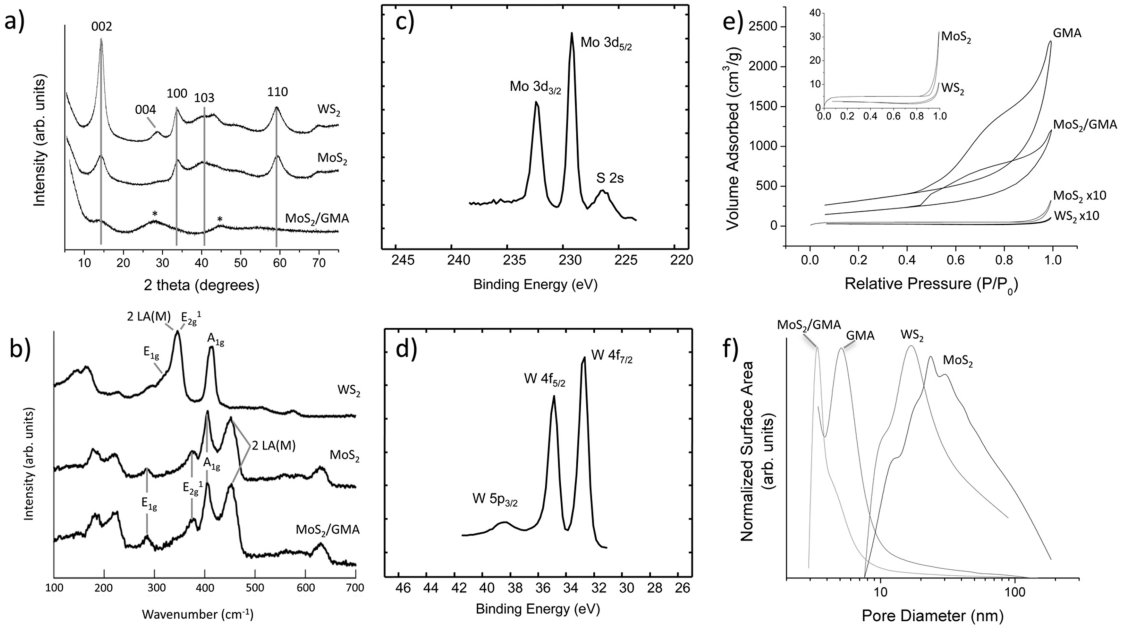

Figure 2. (a) XRD and (b) Raman spectra of WS_2 aerogel, MoS_2 aerogel, and MoS_2/GMA. Asterisks in panel a denote XRD peaks due to GMA. XPS spectra of (c) Mo 3d peaks in MoS_2 and (d) W 4f peaks in WS_2 aerogels. (e) Nitrogen adsorption/desorption isotherms for WS_2 aerogel (×10), MoS_2 aerogel (×10), MoS_2/GMA, and GMA. Inset shows isotherms for MoS_2 and WS_2 aerogels (actual scale). (f) Pore size distribution for WS_2 aerogel, MoS_2 aerogel, MoS_2/GMA, and GMA.

foam structure are replicated in the final WS_2 aerogel morphology.

High-resolution transmission electron microscopy (HRTEM) gives further insight concerning the microstructure of the dichalcogenide aerogels. (Figure 1h–i) Both the MoS_2 and WS_2 aerogel are made up of nanoparticles with a 5–10 nm domain size and 2–6 monolayers thick. The nanoparticles are randomly oriented; however, within each particle, the layers appear crystalline with well-ordered stacking. The X-ray diffraction (XRD) patterns (Figure 2a) and Raman spectra (Figure 2b) confirm both the crystalline nature of the aerogels and the identity of the annealed aerogels as MoS_2 and WS_2. The XRD patterns show the characteristic peaks for MoS_2 and WS_2 (JCPDS-ICDD 37-1492, 8-237). The asymmetry observed in the XRD peaks suggests turbostratic stacking is dominant in both aerogels. Furthermore, while both aerogels exhibit the (002) peak indicating stacked sheets, the weaker (002) peak and the complete absence of the (004) peak in the MoS_2 aerogel suggest less crystallinity (*i.e.*, smaller domains, more sheet curvature).[49,50] This result is consistent with the FE-SEM images (Figure 1d–g) that show much smaller sheets with more curvature in the MoS_2 aerogel than in the WS_2 aerogel. Raman spectra are consistent with randomly oriented nanocrystalline MoS_2 and WS_2.[51−53] The literature describes MoS_2 Raman spectra for bulk single crystals as well as spectral changes due to small domain size and small layer thickness. The major peaks found for the MoS_2 aerogel are A_{1g} (407 cm^{-1}), E_{1g} (284 cm^{-1}), and $E_{2g}{}^1$ (374 cm^{-1}) along with 2xLA(M) at ~450 cm^{-1}. These peak positions are in good agreement with literature values for nanoparticulate MoS_2 that is composed of multiple layers (rather than monolayer). The major peaks found for the WS_2 aerogel are A_{1g} (415 cm^{-1}), E_{1g} (tentatively at 319 cm^{-1}), and $E_{2g}{}^1$ (353 cm^{-1}) along with 2xLA(M) at ~340 cm^{-1}. The peak position for the A_{1g} mode, which is the strongest indicator of coupling between layers, is consistent with literature reports for exfoliated (monolayer) flakes. However, our HRTEM images suggest that particles are composed of multiple layers. Though not definitive, together these findings would suggest stacked flakes that are less coupled (farther apart) than bulk. The peak assigned to A_{1g} may also have a B_{2u} component.[53] This would explain the difference between the peak value near 415 cm^{-1} and the positions of the resonant peaks $A_{1g} \pm$ LA(M), which are consistent with a lower value (see Supporting Information, Figure S3).

X-ray photoelectron spectroscopy (XPS) characterization was performed to determine the oxidation states of the Mo and W in the aerogels. (Figure 2c,d and Supporting Information, Figure S2) According to XPS analysis, 94% of the Mo 3d signal in the MoS_2 aerogel is due to Mo(IV) species in MoS_2 (Mo $3d_{5/2}$, BE = 229.2 eV). Nearly 100% of the sulfur is due to S^{2-} (S $2p_{3/2}$, BE = 162.0 eV) typical of MoS_2, not MoS_3 (162.9 eV).[54] This suggests there is ~6% MoO_3 in the aerogel. For the WS_2 aerogel, nearly 100% of the W 4f signal is due to W(IV) species in WS_2 (W $4f_{7/2}$, BE = 32.8 eV). At the same time, nearly all the S 2p signal is the S^{2-} (S $2p_{3/2}$, BE = 162.4 eV) typical of WS_2.

Nitrogen porosimetry was used to further characterize the textural properties of the dichalcogenide

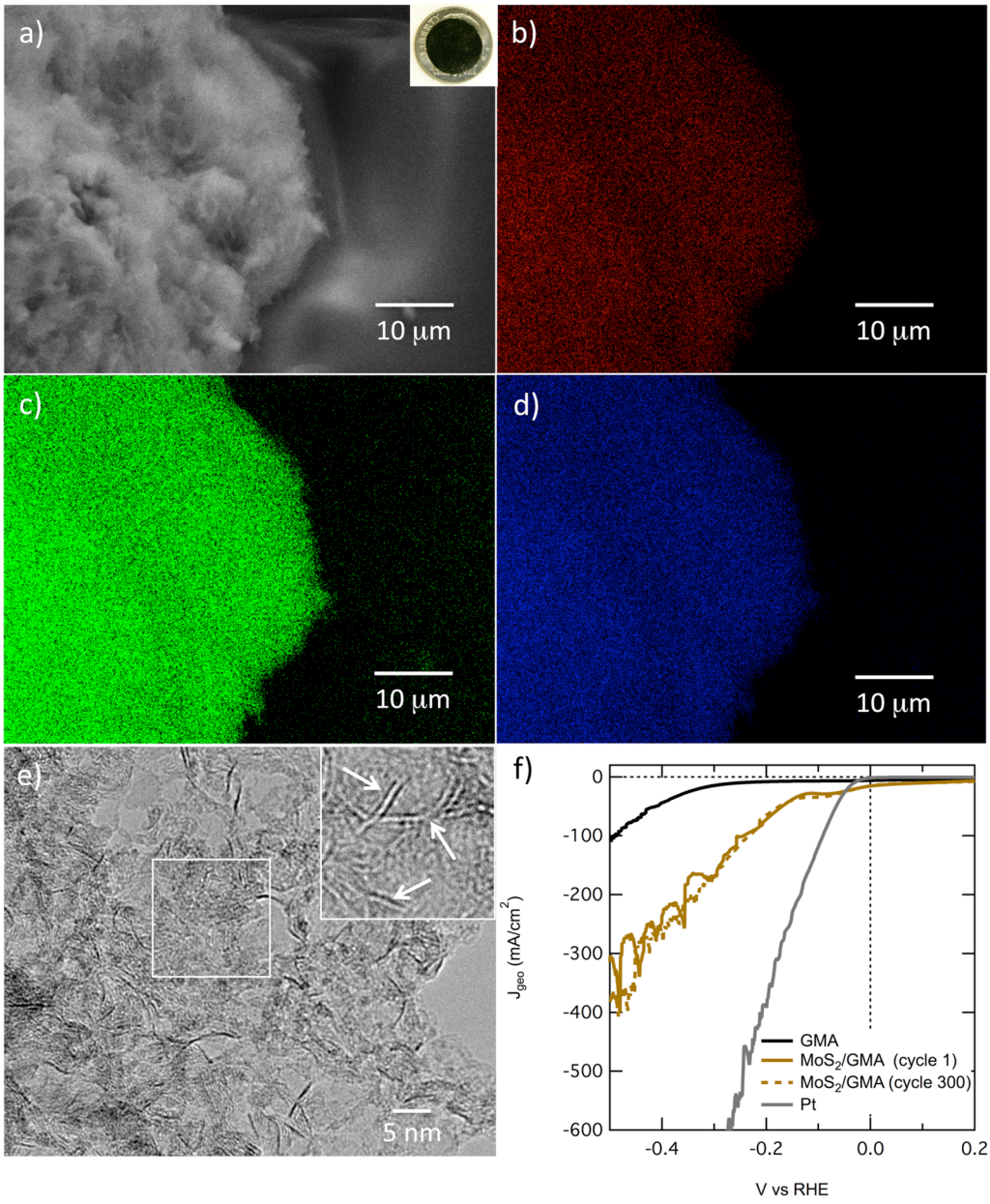

Figure 3. (a) SEM image and EDX element mapping of (b) Mo, (c) S, and (d) C signal in MoS_2/GMA. The inset in panel a is an image of the MoS_2/GMA disk set on a dime. (e) TEM image of MoS_2/GMA. Inset in panel e is magnification of white box defocused to show MoS_2 sheets (arrows). The inset is 15 nm in width. (f) Linear polarization scans for the MoS_2/GMA monolith (brown). The first (solid brown) and 300th (dashed brown) cycles are shown. GMA monolith (black) and a flat, polished platinum standard (gray) are shown for comparison.

aerogels. The nitrogen adsorption/desorption isotherms for the MoS_2 and WS_2 aerogels exhibited the Type 3 hysteresis loop (IUPAC classification) at high relative pressure that is typically associated with adsorption within aggregates of plate-like particles, consistent with the morphology observed in the FE-SEM and HRTEM images. Pore size distributions show broad profiles in the mesopore range with peaks at 20 and 30 nm for the WS_2 and MoS_2 aerogels, respectively. The BET surface area for the MoS_2 and WS_2 aerogels was 18 and 9 m^2/g, respectively. These surface areas are consistent for dichalcogenides synthesized *via* thermal decomposition of ammonium thio-metal salts.[45,55]

For applications, such as catalysis and gas storage, greater specific surface area and electrical conductivity is desirable.[56] To this end, a lightweight, high surface area graphene macro-assembly (GMA)[33] was chosen to support the MoS_2 sheets. The GMA was infiltrated with the ATM solution, freeze-dried, and then annealed at 450 °C under hydrogen to create a MoS_2/graphene hybrid aerogel. The resulting hybrid aerogel, MoS_2/GMA, contained 49 wt % MoS_2, maintained the pore size distribution of the GMA (with a small decrease in peak pore size), and exhibited an extremely high surface area of 691 m^2/g. (Figure 2e,f) The MoS_2/GMA surface area is more than twice as large as the

values reported for other nanostructured MoS_2 materials[4,45,57] and is made possible by the homogeneous distribution of the MoS_2 on the graphene scaffold, as shown *via* SEM and EDX (Figure 3), and the large native surface area of the GMA (~1300 m^2/g, Figure 2e). Furthermore, HRTEM (Figure 3e) shows that the MoS_2 is present in the form of mostly single or few-layer sheets on the GMA. The Raman spectrum being identical to that of the pure MoS_2 aerogel and the XRD spectrum, showing only a weak (002) MoS_2 peak, supports the presence of single and few-layer MoS_2 sheets conformally coating the "wrinkled" graphene substrate (Figure 2a,b).[49,50] Because of the single and few-layer conformal MoS_2 coating, the hybrid aerogel represents the best-case scenario with respect to surface area, 2× increase in mass resulted in only a 50% reduction in the available surface area. In addition, the robust nature of the graphene scaffold allows the hybrid aerogel to retain the native electrical conductivity of the graphene aerogel (1.12 S/cm) in stark contrast to the nonconductive nature of the pure dichalcogenide aerogels. This difference in conductivity meant that only the MoS_2/GMA hybrid could be used in its monolithic form for electrocatalytic testing. Electrodes made from the pure dichalcogenide aerogel powders were unstable and inefficient. (see Supporting Information, Figures S4 and S5).

Linear polarization scans in 0.5 M H_2SO_4 (Figure 3f) were used to extract performance metrics for the MoS_2/GMA such as the onset potential for hydrogen evolution and the potential needed to achieve specific current densities. Because of its large surface area, the MoS_2/GMA has large nonfaradaic contributions (*e.g.*, capacitance) to the current that are distinct from its catalytic activity. (see Supporting Information, Figure S4) Once these nonfaradaic contributions are accounted for, the overpotential needed to generate 10 mA/cm^2 is −0.12 V and the overpotential needed to generate 100 mA/cm^2 is −0.26 V vs RHE. These high current densities greatly exceed those of physical MoS_2/carbon mixtures and are similar to those reported for MoS_2 nanoparticles grown directly on graphene.[56,58] Because of the presence of a redox peak near the onset of hydrogen evolution the onset potential was chosen by extrapolation from the near-vertical portion of the curve rather than the near-horizontal curve (as is more common in the literature). (Supporting Information, Figure S4). This shifts the onset potential to a more negative value compared to other studies. The presence of a redox peak near the onset of hydrogen evolution also prevented a Tafel representation of the data. Despite the shift, the MoS_2/GMA proves to be an efficient H_2 evolution reaction (HER) catalyst operating at potentials similar (−0.10 V) to platinum.[3] This low overpotential is consistent with other reports for MoS_2/graphene catalysts.[56,58] The ~10× lower HER current of the pristine GMA (~10 mA/cm^2 at −0.26 V vs RHE) indicates a lack of catalytic activity and highlights the good catalytic activity of the MoS_2 sheets generated by our method.

To test the robustness of the MoS_2/GMA monoliths, they were continuously cycled in 0.5 M H_2SO_4 at 2 mV/s from 0.4 to −0.7 V vs RHE for 300 cycles. Total cycling time was ~20 h. The current density has significant fluctuations because hydrogen bubbles intermittently block the electrode and then float away. The first and 300th cycle are essentially unchanged demonstrating good stability. (Figure 3f) Impedance measurements (Supporting Information, Figure S6) also show that the capacitance, and hence area, of the MoS_2/GMA did not change during the cycling process.

The high HER catalytic activity of the MoS_2/GMA hybrid aerogel suggests that much of the MoS_2 interfacing with the electrolyte is edge sites and that those sites are in electrical contact with the graphene.[10,56] Beyond HER, the presence of the conductive graphene support in the hybrid material has the potential to significantly improve performance *via* electrochemical promotion of catalysis (EPOC).[59] Though EPOC has shown up to 5 orders of magnitude increases in activity over open circuit values and has been noted in more than 80 systems, it has not yet been used in commercial systems largely due to the difficulty and expense of making porous metal substrates. Therefore, cost-effective carbon-based substrates could have broad implications in the field of catalysis by expanding the use of EPOC to industrial settings. Catalytic studies are the subject of ongoing research.

CONCLUSIONS

In summary, we have presented a facile method for the fabrication of ultralow-density layered dichalcogenide and dichalcogenide/graphene aerogels. Our synthesis scheme relies on the 3D assembly of metal chalcogenide precursors into stable 3D architectures that are robust enough to maintain their monolithic structures during freeze-drying and thermal decomposition to the dichalcogenide aerogel. The resulting MoS_2 and WS_2 aerogels were extremely low in density (0.4% and 0.5% theoretical maximum density, respectively) and displayed Young's moduli on the order of graphene aerogels. The MoS_2/GMA exhibited very large surface areas (~700 m^2/g), high electrical conductivity, and good activity as an HER catalyst. There have been several reports[3,19,56,58,60,61] of HER enhancement from MoS_2; many of these are MoS_2 mixed with carbon black[3,61] or deposited on graphite[60] to allow a voltage to be applied. The distinguishing features of this work are the (a) intimate bonding and the dispersion of the MoS_2 (as evidenced by the TEM and EDX); (b) the exceptionally high surface area

support in contact with the solution (as evidenced by the catalytic activity); and (c) the high conductivity of the graphene aerogel backbone (2 times higher than activated carbon). Furthermore, the synthesis approach allows fabrication as conformable monoliths with macroscopic dimensions. Therefore, the method described here provides the blueprint for realizing a whole new class of ultralow-density, nanostructured materials for future catalysis and energy storage applications.

METHODS

MoS_2 and WS_2 Aerogel. In a typical synthesis, 26 mg of ammonium thio-molybdate (ATM) or 36 mg of ammonium thio-tungstate (ATT) is dissolved in 1 mL of deionized water in a vial. The vial is then submerged in liquid nitrogen to rapidly freeze the solution. The frozen solution is then placed under vacuum (freeze-dried) to produce an ATM or ATT aerogel. The ATM or ATT aerogel is annealed in 2% H_2/98% inert gas mixture at 450 °C for 4 h to yield the MoS_2 or WS_2 aerogel.

MoS_2/GMA Hybrid Aerogel. GMA is synthesized according to the literature method.[33] The GMA is immersed in the aqueous ATM solution described for making the MoS_2 aerogel. From here, the ATM-infiltrated GMA is processed in exactly the same manner as prescribed for the MoS_2 aerogel to yield the MoS_2/GMA hybrid aerogel.

Electron Microscopy. Field-emission scanning electron microscopy (FE-SEM) and energy dispersive X-ray (EDX) analysis was performed on a JEOL 7401-F at 10 keV (20 mA) in lower secondary electron imaging mode with a working distance of 2−8 mm. High resolution transmission electron microscopy (HRTEM) characterization was performed on a FEI TF-20 Tecnai electron microscope operated at 200 kV.

X-ray Photoelectron Spectroscopy. X-ray photoelectron spectroscopy (XPS) was performed on a PHI Quantum 2000 system using a focused monochromatic Al Kα X-ray source (1486.6 eV) for excitation and a spherical section analyzer with 16-element multichannel detection system. The X-ray beam is incident normal to the sample and the detector is 45° from normal. Spectra were collected with a 200 μm X-ray spot using a pass energy of 23.5 eV, giving an energy resolution of 0.3 eV that when combined with the 0.85 eV full width half-maximum (fwhm) Al Kα line width gives a resolvable XPS peak width of 1.2 eV. Deconvolution of nonresolved peaks was accomplished using Multipak 9.2 (PHI) curve fitting routines with asymmetric or Gaussian−Lorentzian line-shapes and a Shirley background. The collected data were referenced to an energy scale with binding energies for Cu $2p_{3/2}$ at 932.72 ± 0.05 eV and Au $4f_{7/2}$ at 84.01 ± 0.05 eV. Binding energies were also referenced to the C 1s photoelectron line arising from adventitious carbon at 284.6 eV. Low energy electrons and ions were used for specimen neutralization.

Nitrogen Porosimetry. Textural properties were determined by Brunauer−Emmett−Teller (BET) and Barrett−Joyner−Halenda (BJH) methods using an ASAP 2020 surface area analyzer (Micromeritics Instrument Corporation) *via* nitrogen porosimetry.[62] Samples of approximately 0.1 g were heated to 150 °C under vacuum (10^{-5} Torr) for at least 24 h to remove all adsorbed species.

X-ray Diffraction. X-ray diffraction (XRD) measurements were performed on a Bruker AXS D8 ADVANCE X-ray diffractometer equipped with a LynxEye 1-dimensional linear Si strip detector. The samples were scanned from 5 to 75° 2θ. The step scan parameters were 0.02° steps and 2 s counting time per step with a 0.499° divergence slit and a 0.499° antiscatter slit. The X-ray source was Ni-filtered Cu radiation from a sealed tube operated at 40 kV and 40 mA. Phases in the samples were identified by comparison of observed peaks to those in the International Centre for Diffraction Data (ICDD PDF2009) powder diffraction database, and also peaks listed in reference articles. Goniometer alignment was ensured using a Bruker-supplied Al_2O_3 standard.

Raman Spectroscopy. Raman spectra were obtained using a Thermo Nicolet Almega Confocal Raman spectrometer equipped with an Olympus microscope, and a 632.8 nm HeNe laser as the excitation source. Sixteen scans with 10 s collection times were obtained for each spectrum in the 100−3900 cm^{-1} range. The spectrometer was calibrated using a silicon standard, with a strong primary band at 520.5 cm^{-1}. Peak positions were fit assuming a Lorentz peak shape and a linear background. The 633 nm (1.96 eV) excitation frequency is near the "A" exciton absorption lines for both MoS_2 (1.88 eV)[63] and WS_2 (1.95 eV).[52] This induces second-order Raman scattering due to the coupling of primary electronic excitations with phonon modes.

Nanoindentation. The samples were indented in the load-controlled mode in an MTS XP nanoindenter with a Berkovich diamond tip. Elastic properties are characterized by the Young's modulus, which was calculated based on the initial slope of the unloading curve according to the Oliver−Pharr method.[64] In Oliver−Pharr calculations, we assumed Poisson's ratios of diamond and the graphene assemblies of 0.07 and 0.2, respectively, and the Young's modulus of diamond of 1141 GPa.[65] Several (>10) indentations were performed on different sample locations and loading directions, and results were averaged. Standard deviation error was ±10%.

Electrical Conductivity. Electrical conductivity was measured using the four-probe method with metal electrodes attached to the samples. The amount of current transmitted through the sample during measurement was 100 mA, and the voltage drop along the various sample axes was measured over distances of 3 to 6 mm. Seven or more measurements were taken on each sample, and the results were averaged.

Density. Bulk densities of the samples were determined from the physical dimensions and mass of each sample.

Electrochemical Characterization. All electrochemical tests were performed in 0.5 M H_2SO_4 using a BioLogic SP300 potentiostat. Solutions were purged with argon gas (99.99999%) for at least 20 min before testing and for the duration of the measurements. All measurements used *iR* compensation. Typical resistances were 4−6 ohms. In addition, nonfaradaic contributions to the current are estimated for the monolith samples and subtracted before extracting performance metrics. Scan rates are 2 mV/s for MoS_2/GMA, 5 mV/s for GMA, and 50 mV/s for platinum. To partially remove H_2 bubbles the monoliths are mounted at a 45 deg angle, whereas the platinum sample is mounted vertically and rotated at 2500 rpm. The working electrodes, counter electrodes, and reference electrodes are described in the following sections.

Working Electrodes. Disks of ~8 mm diameter were placed within a PEEK cell (Asylum Research) exposing a 5 mm diameter face (0.196 cm^2). Owing to the porous nature of the monoliths, a custom graphite holder was used to ensure that solution only wetted graphite or the aerogel. MoS_2/GMA samples were ~1 mm thick and weighed ~0.04 g (or 0.2 g/cm^2). Thinner 100 μm GMA monolith electrodes weighed ~0.004 g (or 0.002 g/cm^2). Measured weights of each sample (±0.0001 g) were used to normalize the capacitance. A polished, 5 mm diameter platinum disk electrode (Pine Instruments AFE5T050PT) was used as the Pt standard.

Reference and Counter Electrodes. For stability studies we used a 99.9995% graphite counter electrode (Alfa Aesar 14738) and a double junction calomel reference electrode (Hach REF451) with the outer junction filled with 0.5 M H_2SO_4. The calomel (SCE) reference electrode was calibrated with respect to the $Hg/HgSO_4$ electrode in H_2 saturate solution as described above. The offset with respect to normal hydrogen electrode was estimated from the solution pH = 0.41 ± 0.02 using, V(RHE) = V(NHE) − 0.059·pH. The pH was measured using a freshly calibrated double junction pH probe (Accumet model 13-620-183a). Numerically, V(RHE) = V(SCE) + 0.267 and V(RHE) = V(NHE) − 0.024 ± 0.001.

Conflict of Interest: The authors declare no competing financial interest.

Acknowledgment. This work was performed under the auspices of the U.S. Department of Energy by Lawrence Livermore National Laboratory under Contract DE-AC52-07NA27344. Transmission electron microscopy experiments were conducted at the National Center for Electron Microscopy, Lawrence Berkeley National Laboratory, which is supported by the U.S. Department of Energy under Contract DE-AC02-05CH11231. Funding was provided by the UC Lab Fees Research Program under Award 12-LR-235323, and the Lawrence Livermore National Laboratory Directed Research and Development (LDRD) Grant 13-LW-099.

Supporting Information Available: Load vs displacement plot for dichalcogenide aerogel; XPS spectra and peak fitting; Raman spectra; linear polarization curves; cyclic voltammetry plots; electrochemical impedance spectra; supporting methods and discussion. This material is available free of charge *via* the Internet at http://pubs.acs.org

REFERENCES AND NOTES

1. Rapoport, L.; Bilik, Y.; Feldman, Y.; Homyonfer, M.; Cohen, S. R.; Tenne, R. Hollow Nanoparticles of WS_2 as Potential Solid-State Lubricants. *Nature* **1997**, *387*, 791–793.
2. Chen, J.; Kuriyama, N.; Yuan, H.; Takeshita, H. T.; Sakai, T. Electrochemical Hydrogen Storage in MoS_2 Nanotubes. *J. Am. Chem. Soc.* **2001**, *123*, 11813–11814.
3. Jaramillo, T. F.; Jorgensen, K. P.; Bonde, J.; Nielsen, J. H.; Horch, S.; Chorkendorff, I. Identification of Active Edge Sites for Electrochemical H_2 Evolution from MoS_2 Nanocatalysts. *Science* **2007**, *317*, 100–102.
4. Yoosuk, B.; Kim, J. H.; Song, C.; Ngamcharussrivichai, C.; Prasassarakich, P. Highly Active MoS_2, $CoMoS_2$, and $NiMoS_2$ Unsupported Catalysts Prepared by Hydrothermal Synthesis for Hydrodesulfurization of 4,6-Dimethyldibenzothiophene. *Catal. Today* **2008**, *130*, 14–23.
5. Lebegue, S.; Eriksson, O. Electronic Structure of Two-Dimensional Crystals from ab Initio Theory. *Phys. Rev. B* **2009**, 79.
6. Mak, K. F.; Lee, C.; Hone, J.; Shan, J.; Heinz, T. F. Atomically Thin MoS_2: A New Direct-Gap Semiconductor. *Phys. Rev. Lett.* **2010**, 105.
7. Matte, H.; Gomathi, A.; Manna, A. K.; Late, D. J.; Datta, R.; Pati, S. K.; Rao, C. N. R. MoS_2 and WS_2 Analogues of Graphene. *Angew. Chem., Int. Ed.* **2010**, *49*, 4059–4062.
8. Splendiani, A.; Sun, L.; Zhang, Y. B.; Li, T. S.; Kim, J.; Chim, C. Y.; Galli, G.; Wang, F. Emerging Photoluminescence in Monolayer MoS_2. *Nano Lett.* **2010**, *10*, 1271–1275.
9. Coleman, J. N.; Lotya, M.; O'Neill, A.; Bergin, S. D.; King, P. J.; Khan, U.; Young, K.; Gaucher, A.; De, S.; Smith, R. J.; et al. Two-Dimensional Nanosheets Produced by Liquid Exfoliation of Layered Materials. *Science* **2011**, *331*, 568–571.
10. Kibsgaard, J.; Chen, Z. B.; Reinecke, B. N.; Jaramillo, T. F. Engineering the Surface Structure of MoS_2 to Preferentially Expose Active Edge Sites for Electrocatalysis. *Nat. Mater.* **2012**, *11*, 963–969.
11. Wang, Q. H.; Kalantar-Zadeh, K.; Kis, A.; Coleman, J. N.; Strano, M. S. Electronics and Optoelectronics of Two-Dimensional Transition Metal Dichalcogenides. *Nat. Nanotechnol.* **2012**, *7*, 699–712.
12. Balendhran, S.; Walia, S.; Nili, H.; Ou, J. Z.; Zhuiykov, S.; Kaner, R. B.; Sriram, S.; Bhaskaran, M.; Kalantar-zadeh, K. Two-Dimensional Molybdenum Trioxide and Dichalcogenides. *Adv. Funct. Mater.* **2013**, *23*, 3952–3970.
13. Butler, S. Z.; Hollen, S. M.; Cao, L. Y.; Cui, Y.; Gupta, J. A.; Gutierrez, H. R.; Heinz, T. F.; Hong, S. S.; Huang, J. X.; Ismach, A. F.; *et al*. Progress, Challenges, and Opportunities in Two-Dimensional Materials Beyond Graphene. *ACS Nano* **2013**, *7*, 2898–2926.
14. Chhowalla, M.; Shin, H. S.; Eda, G.; Li, L. J.; Loh, K. P.; Zhang, H. The Chemistry of Two-Dimensional Layered Transition Metal Dichalcogenide Nanosheets. *Nat. Chem.* **2013**, *5*, 263–275.
15. Huang, X.; Zeng, Z. Y.; Zhang, H. Metal Dichalcogenide Nanosheets: Preparation, Properties and Applications. *Chem. Soc. Rev.* **2013**, *42*, 1934–1946.
16. Tang, Q.; Zhou, Z. Graphene-Analogous Low-Dimensional Materials. *Prog. Mater. Sci.* **2013**, *58*, 1244–1315.
17. Xu, M. S.; Liang, T.; Shi, M. M.; Chen, H. Z. Graphene-like Two-Dimensional Materials. *Chem. Rev.* **2013**, *113*, 3766–3798.
18. Huang, X.; Tan, C.; Yin, Z.; Zhang, H. 25th Anniversary Article: Hybrid Nanostructures Based on Two-Dimensional Nanomaterials. *Adv. Mater.* **2014**, *26*, 2185–2204.
19. Merki, D.; Hu, X. L. Recent Developments of Molybdenum and Tungsten Sulfides as Hydrogen Evolution Catalysts. *Energy Environ. Sci.* **2011**, *4*, 3878–3888.
20. Harley-Trochimczyk, A.; Chang, J.; Zhou, Q.; Dong, J.; Pham, T.; Worsley, M. A.; Maboudian, R.; Zettl, A.; Mickelson, W. Catalytic Hydrogen Sensing Using Microheated Platinum Nanoparticle-Loaded Graphene Aerogel. *Sens. Actuat. B, Chem.* **2015**, *206*, 399–406.
21. Chen, W.; Yan, L. In Situ Self-Assembly of Mild Chemical Reduction Graphene for Three-Dimensional Architectures. *Nanoscale* **2011**, *3*, 3132–3137.
22. Chen, Z. P.; Ren, W. C.; Gao, L. B.; Liu, B. L.; Pei, S. F.; Cheng, H. M. Three-Dimensional Flexible and Conductive Interconnected Graphene Networks Grown by Chemical Vapour Deposition. *Nat. Mater.* **2011**, *10*, 424–428.
23. Lin, Y.; Ehlert, G. J.; Bukowsky, C.; Sodano, H. A. Superhydrophobic Functionalized Graphene Aerogels. *ACS Appl. Mater. Interfaces* **2011**, *3*, 2200–2203.
24. Sun, Y. Q.; Wu, Q. O.; Shi, G. Q. Graphene Based New Energy Materials. *Energy Environ. Sci.* **2011**, *4*, 1113–1132.
25. Worsley, M. A.; Olson, T. Y.; Lee, J. R. I.; Willey, T. M.; Nielsen, M. H.; Roberts, S. K.; Pauzauskie, P. J.; Biener, J.; Satcher, J. H.; Baumann, T. F. High Surface Area, Sp2-Cross-Linked Three-Dimensional Graphene Monoliths. *J. Phys. Chem. Lett.* **2011**, *2*, 921–925.
26. Yang, X.; Qiu, L.; Cheng, C.; Wu, Y.; Ma, Z.-F.; Li, D. Ordered Gelation of Chemically Converted Graphene for Next-Generation Electroconductive Hydrogel Films. *Angew. Chem., Int. Ed.* **2011**, *50*, 7325–7328.
27. Zhang, X.; Sui, Z.; Xu, B.; Yue, S.; Luo, Y.; Zhan, W.; Liu, B. Mechanically Strong and Highly Conductive Graphene Aerogel and Its Use as Electrodes for Electrochemical Power Sources. *J. Mater. Chem.* **2011**, *21*, 6494–6497.
28. Bi, H.; Yin, K.; Xie, X.; Zhou, Y.; Wan, N.; Xu, F.; Banhart, F.; Sun, L.; Ruoff, R. S. Low Temperature Casting of Graphene with High Compressive Strength. *Adv. Mater.* **2012**, *24*, 5124–5129.
29. Biener, J.; Dasgupta, S.; Shao, L.-H.; Wang, D.; Worsley, M. A.; Wittstock, A.; Lee, J. R. I.; Biener, M. M.; Orme, C. A.; Kucheyev, S. O.; *et al*. Macroscopic 3d Nanographene with Dynamically Tunable Bulk Properties. *Adv. Mater.* **2012**, *24*, 5083–5087.
30. Niu, Z.; Chen, J.; Hng, H. H.; Ma, J.; Chen, X. A Leavening Strategy to Prepare Reduced Graphene Oxide Foams. *Adv. Mater.* **2012**, 4144–4150.
31. Qiu, L.; Liu, J. Z.; Chang, S. L. Y.; Wu, Y. Z.; Li, D. Biomimetic Superelastic Graphene-Based Cellular Monoliths. *Nat. Commun.* **2012**, 3.
32. Tang, L. A. L.; Lee, W. C.; Shi, H.; Wong, E. Y. L.; Sadovoy, A.; Gorelik, S.; Hobley, J.; Lim, C. T.; Loh, K. P. Highly Wrinkled Cross-Linked Graphene Oxide Membranes for Biological and Charge-Storage Applications. *Small* **2012**, *8*, 423–431.
33. Worsley, M. A.; Kucheyev, S. O.; Mason, H. E.; Merrill, M. D.; Mayer, B. P.; Lewicki, J.; Valdez, C. A.; Suss, M. E.; Stadermann, M.; Pauzauskie, P. J.; et al. Mechanically Robust 3D Graphene Macroassembly with High Surface Area. *Chem. Commun.* **2012**, *48*, 8428–8430.
34. Yin, S.; Niu, Z.; Chen, X. Assembly of Graphene Sheets into 3d Macroscopic Structures. *Small* **2012**, *8*, 2458.
35. Zhang, L. L.; Zhao, X.; Stoller, M. D.; Zhu, Y. W.; Ji, H. X.; Murali, S.; Wu, Y. P.; Perales, S.; Clevenger, B.; Ruoff, R. S. Highly Conductive and Porous Activated Reduced Graphene Oxide Films for High-Power Supercapacitors. *Nano Lett.* **2012**, *12*, 1806–1812.

36. Cheng, W.-Y.; Wang, C.-C.; Lu, S.-Y. Graphene Aerogels as a Highly Efficient Counter Electrode Material for Dye-Sensitized Solar Cells. *Carbon* **2013**, *54*, 291–299.
37. Lin, Z.; Waller, G. H.; Liu, Y.; Liu, M.; Wong, C.-p. 3d Nitrogen-Doped Graphene Prepared by Pyrolysis of Graphene Oxide with Polypyrrole for Electrocatalysis of Oxygen Reduction Reaction. *Nano Energy* **2013**, *2*, 241–248.
38. Sun, H.; Xu, Z.; Gao, C. Multifunctional, Ultra-flyweight, Synergistically Assembled Carbon Aerogels. *Adv. Mater.* **2013**, *25*, 2554–2560.
39. Zhao, Y.; Liu, J.; Hu, Y.; Cheng, H. H.; Hu, C. G.; Jiang, C. C.; Jiang, L.; Cao, A. Y.; Qu, L. T. Highly Compression-Tolerant Supercapacitor Based on Polypyrrole-Mediated Graphene Foam Electrodes. *Adv. Mater.* **2013**, *25*, 591–595.
40. Worsley, M. A.; Charnvanichborikarn, S.; Montalvo, E.; Shin, S. J.; Tylski, E. D.; Lewicki, J. P.; Nelson, A. J.; Satcher, J. H.; Biener, J.; Baumann, T. F.; et al. Toward Macroscale, Isotropic Carbons with Graphene-Sheet-like Electrical and Mechanical Properties. *Adv. Funct. Mater.* **2014**, 4259–4264.
41. Mohanan, J. L.; Arachchige, I. U.; Brock, S. L. Porous Semiconductor Chalcogenide Aerogels. *Science* **2005**, *307*, 397–400.
42. Yin, J.; Li, X.; Zhou, J.; Guo, W. Ultralight Three-Dimensional Boron Nitride Foam with Ultralow Permittivity and Superelasticity. *Nano Lett.* **2013**, *13*, 3232–3236.
43. Rousseas, M.; Goldstein, A. P.; Mickelson, W.; Worsley, M. A.; Woo, L.; Zettl, A. Synthesis of Highly Crystalline sp^2-Bonded Boron Nitride Aerogels. *ACS Nano* **2013**, *7*, 8540–8546.
44. Jung, S. M.; Jung, H. Y.; Dresselhaus, M. S.; Jung, Y. J.; Kong, J. A Facile Route for 3d Aerogels from Nanostructured 1d and 2d Materials. *Sci. Rep.* **2012**, 2.
45. Soto-Puente, M.; Valle, M.; Flores-Aquino, E.; Avalos-Borja, M.; Fuentes, S.; Cruz-Reyes, J. Synthesis, Characterization and Cyclohexene Hydrogenation Activity of High Surface Area Molybdenum Disulfide Catalysts. *Catal. Lett.* **2007**, *113*, 170–175.
46. Wilkinson, K.; Merchan, M. D.; Vasudevan, P. T. Characterization of Supported Tungsten Sulfide Catalysts Ex Ammonium Tetrathiotungstate. *J. Catal.* **1997**, *171*, 325–328.
47. Huang, W. M.; Ding, Z.; Wang, C. C.; Wei, J.; Zhao, Y.; Purnawali, H. Shape Memory Materials. *Mater. Today* **2010**, *13*, 54–61.
48. Worsley, M. A.; Pauzauskie, P. J.; Olson, T. Y.; Biener, J.; Satcher, J. H.; Baumann, T. F. Synthesis of Graphene Aerogel with High Electrical Conductivity. *J. Am. Chem. Soc.* **2010**, *132*, 14067–14069.
49. Liang, K. S.; Chianelli, R. R.; Chien, F. Z.; Moss, S. C. Structure of Poorly Crystalline MoS_2—A Modeling Study. *J. Non · Cryst. Solids* **1986**, *79*, 251–273.
50. Ramakrishna, M.; Gomathi, A.; Manna, A. MoS(2) and WS(2) Analogues of Graphene. *Angew. Chem., Int. Ed.* **2010**, *49*, 4059–4062.
51. Zhan, Y.; Liu, Z.; Najmaei, S.; Ajayan, P. M.; Lou, J. Large Area Vapor Phase Growth and Characterization of MoS_2 Atomic Layers on SiO_2 Substrate. *Small* **2012**, *8*, 966–971.
52. Fan, J.-H.; Gao, P.; Zhang, A.-M.; Zhu, B.-R.; Zeng, H.-L.; Cui, X.-D.; He, R.; Zhang, Q.-M. Resonance Raman Scattering in Bulk 2H-MX_2 (M = Mo, W; X = S, Se) and Monolayer MoS_2. *J. Appl. Phys.* **2014**, *115*, 053527.
53. Zhao, W. J.; Ghorannevis, Z.; Amara, K. K.; Pang, J. R.; Toh, M.; Zhang, X.; Kloc, C.; Tan, P. H.; Eda, G. Lattice Dynamics in Mono- and Few-Layer Sheets of WS_2 and WSe_2. *Nanoscale* **2013**, *5*, 9677–9683.
54. Weber, T.; Muijsers, J. C.; Niemantsverdriet, J. W. Structure of Amorphous MoS_3. *J. Phys. Chem.* **1995**, *99*, 9194–9200.
55. Alonso-Nunez, G.; Huirache-Acuna, R.; Paraguay-Delgado, F.; Lumbreras, J. A.; Garcia-Alamilla, R.; Castillo-Mares, A.; Romero, R.; Somanathan, R.; Chianelli, R. R. Synthesis and Characterization of Hexamethylenediammonium Thiometallates as Precursors of MoS_2 and WS_2 Catalysts: In Situ Activation during HDS of DBT. *Catal. Lett.* **2009**, *130*, 318–326.
56. Liao, L.; Zhu, J.; Bian, X. J.; Zhu, L. N.; Scanlon, M. D.; Girault, H. H.; Liu, B. H. MoS_2 Formed on Mesoporous Graphene as a Highly Active Catalyst for Hydrogen Evolution. *Adv. Funct. Mater.* **2013**, *23*, 5326–5333.
57. Li, N.; Chai, Y.; Dong, B.; Liu, B.; Guo, H.; Liu, C. Preparation of Porous MoS_2 *via* a Sol−Gel Route Using $(NH_4)_2Mo_3S_{13}$ as Precursor. *Mater. Lett.* **2012**, *88*, 112–115.
58. Li, Y.; Wang, H.; Xie, L.; Liang, Y.; Hong, G.; Dai, H. MoS_2 Nanoparticles Grown on Graphene: An Advanced Catalyst for the Hydrogen Evolution Reaction. *J. Am. Chem. Soc.* **2011**, *133*, 7296–7299.
59. Katsaounis, A. Recent Developments and Trends in the Electrochemical Promotion of Catalysis (EPOC). *J. Appl. Electrochem.* **2010**, *40*, 885–902.
60. Hinnemann, B.; Moses, P. G.; Bonde, J.; Jorgensen, K. P.; Nielsen, J. H.; Horch, S.; Chorkendorff, I.; Norskov, J. K. Biomimetic Hydrogen Evolution: MoS_2 Nanoparticles as Catalyst for Hydrogen Evolution. *J. Am. Chem. Soc.* **2005**, *127*, 5308–5309.
61. Sobczynski, A. Molybdenum Disulfide as a Hydrogen Evolution Catalyst for Water Photodecomposition on Semiconductors. *J. Catal.* **1991**, *131*, 156–166.
62. Gregg, S. J.; Sing, K. S. W. *Adsorption, Surface Area, and Porosity*, 2nd ed.; Academic: London, 1982.
63. Roxlo, C. B.; Chianelli, R. R.; Deckman, H. W.; Ruppert, A. F.; Wong, P. P. Bulk and Surface Optical Absorption in Molybdenum Sulfide. *J. Vac. Sci. Technol. A* **1987**, *5*, 555–557.
64. Oliver, W. C.; Pharr, G. M. An Improved Technique for Determining Hardness and Elastic-Modulus Using Load and Displacement Sensing Indentation Experiments. *J. Mater. Res.* **1992**, *7*, 1564–1583.
65. Kucheyev, S. O.; Hamza, A. V.; Satcher, J. H.; Worsley, M. A. Depth-Sensing Indentation of Low-Density Brittle Nanoporous Solids. *Acta Mater.* **2009**, *57*, 3472–3480.